RSC Advances

PAPER

View Article Online
View Journal | View Issue



Cite this: *RSC Adv.*, 2017, **7**, 10064

# Low-temperature fabrication of $Bi_{25}FeO_{40}$/rGO nanocomposites with efficient photocatalytic performance under visible light irradiation

Xingfu Wang,[ab] Weiwei Mao,[ab] Qi Wang,[a] Yiyi Zhu,[a] Yonggang Min,[a] Jian Zhang,[a] Tao Yang,[a] Jianping Yang,[b] Xing'ao Li*[ab] and Wei Huang*[ac]

Received 19th November 2016
Accepted 30th January 2017

DOI: 10.1039/c6ra27025e

rsc.li/rsc-advances

Bismuth ferrite/reduced graphene oxide ($Bi_{25}FeO_{40}$/rGO) nanocomposites have been synthesized by a hydrothermal method, followed by a simple room temperature liquid phase process. Interestingly, X-ray diffraction and scanning electron microscopy analyses indicated that the presence of rGO triggered the transformation of perovskite phase $BiFeO_3$ to sillenite phase $Bi_{25}FeO_{40}$ at room temperature, while the spindle-like morphology was maintained. Under visible light irradiation, the obtained $Bi_{25}FeO_{40}$/rGO nanocomposites exhibit high photocatalytic performance for the degradation of methyl orange (MO), suggesting potential applications in photocatalytic and related areas. Furthermore, the function of rGO for the enhancement of photocatalytic activity and the probable mechanism were also discussed on the basis of the results.

## 1. Introduction

Bismuth ferrites, a large family of transition-metal oxides, have recently attracted great interest due to their fascinating fundamental physics and extensive technical applications.[1–3] $BiFeO_3$ is known to be a typical perovskite-type bismuth ferrite with simultaneous ferroelectric and ferromagnetic ordering at room temperature.[4–6] With a relatively narrow band gap of ~2.2 eV,[7,8] $BiFeO_3$ is also an important visible-light responsive photocatalyst for the degradation of organic pollutants and water splitting according to recent studies.[9–12] In our previous work, we successfully synthesized $BiFeO_3$ nanostuctures with enhanced photocatalytic activities *via* a facile one-pot hydrothermal approach.[13] However, phase pure $BiFeO_3$ is very difficult to synthesize and a slight impurity phase $Bi_{25}FeO_{40}$ as a by-product is often present.[14,15] Shen *et al.* found that mixed phases of $Bi_{25}FeO_{40}$ and the perovskite type compound of $BiFeO_3$ were obtained in the hydrothermal process.[16] Xu *et al.* have developed a facile hydrothermal method to prepare single-crystal $BiFeO_3$ microplates, where the $Bi_{25}FeO_{40}$ phases firstly formed at the initial stage. With the extension of reaction time, the original $Bi_{25}FeO_{40}$ phases can transform to rhombohedral phases gradually.[17]

Compared to perovskite-type $BiFeO_3$, there has seldom research focus on the optical properties of $Bi_{25}FeO_{40}$ in previous studies. Top seeded solution growth technique has been used to produce $Bi_{25}FeO_{40}$ single crystals for the first time and the optical absorption measurements were performed in a broad spectral (IR, VIS and UV).[18] With a low band gap of 1.8 eV, $Bi_{25}FeO_{40}$ was thought to be a promising visible-light response material.[19] As a representative sillenite-type compound, $Bi_{25}FeO_{40}$ also displayed photocatalytic activity for the degradation of organic dyes under visible-light irradiation.[20,21] It should be emphasized that $Bi_{25}FeO_{40}$ was found to be superparamagnetic,[22] providing the photocatalyst with an extra advantage for feasible separation and recovery.

The combination of the photocatalyst with carbon material to design relevant nanocomposites catalyst can effectively enhance the photocatalytic activity. For example, Li *et al.* have successfully synthesized a novel g-$C_3N_4$/$BiFeO_3$ nanocomposite photocatalyst by a simple hydrothermal method.[23] The as-prepared 50% g-$C_3N_4$/$BiFeO_3$ composites exhibit high efficiency for the degradation of methyl orange (MO) under visible light irradiation. Besides, He *et al.* have successfully fabricated bismuth ferrite/graphene composites *via* a facile and effective two-step hydrothermal treatment which exhibit improved photo-degradation activity toward Congo red.[24]

Graphene is the most important 2-dimensional carbon nanomaterial, which has attracted significant attention owing to the advantages of large surface area and excellent conductivity.[25–27] However, there exists relatively weak interaction and inadequate interfacial contact between the semiconductor and graphene. Notably, reduced graphene oxide (rGO) with oxygen-containing functional groups shows intimate interfacial contact

[a]*Key Laboratory for Organic Electronics & Information Displays (KLOEID), Institute of Advanced Materials (IAM), School of Materials Science and Engineering (SMSE), Nanjing University of Posts and Telecommunications (NUPT), Nanjing 210023, PR China. E-mail: lxahbmy@126.com; iamwhuang@njupt.edu.cn*

[b]*School of Science, Advanced Energy Technology Center, Nanjing University of Posts and Telecommunications (NUPT), Nanjing 210023, PR China*

[c]*Key Laboratory of Flexible Electronics (KLOFE), Institute of Advanced Materials (IAM), National Synergistic Innovation Center for Advanced Materials (SICAM), Nanjing Tech University (NanjingTech), 30 South Puzhu Road, Nanjing 211816, China*

and strong interaction with semiconductors. In this work, the novel $Bi_{25}FeO_{40}$/rGO photocatalysts were successfully synthesized *via* a two-step green liquid phase approach. The $Bi_{25}FeO_{40}$ nanoparticles with homogeneously morphology decorated on the surfaces of the rGO nanosheets. The spindle-like morphology of $Bi_{25}FeO_{40}$ was reported for the first time. Interestingly, at room temperature, a phase transition from rhombohedral to sillenite took place with adding rGO in the solution, while the spindle-like structures were maintained after the reaction. The phase transition at room temperature is significant for its potential applications.

## 2. Experimental section

### 2.1. Fabrication of $Bi_{25}Fe_{40}$/rGO nanocomposites

Bismuth nitrate pentahydrate ($Bi(NO_3)_3 \cdot 5H_2O$) was purchased from Guangdong Xilong Chemical Co., Ltd., P. R. China. Ferric chloride hexahydrate ($FeCl_3 \cdot 6H_2O$), sodium hydroxide (NaOH), methyl orange (MO) and polyvinylpyrrolidone K-30 (PVP) were obtained from Sinopharm Chemical Reagent Corp, P. R. China. All chemicals were used as received without further purification.

Graphene oxide (GO) was synthesized according to the method reported by Hummers and Offeman.[28] Precursors of $BiFeO_3$ were then synthesized by a modified co-precipitation method according to our previous reports.[23]

The typical preparation of $Bi_{25}FeO_{40}$/rGO nanocomposite photocatalysts was as follows: an appropriate amount of $BiFeO_3$ and rGO were completely dispersed in methanol assisted by ultrasonication for 3 h, respectively. The as-prepared $BiFeO_3$ solution and rGO solution were mixed together and stirred in a fume hood for 24 h. After volatilization of the methanol, an opaque powder was obtained after drying at 80 °C in air. The $Bi_{25}FeO_{40}$/rGO photocatalysts with varied $BiFeO_3$ contents (10, 20, 30, 50 wt%) were synthesized, which were denoted as BG1, BG2, BG3 and BG5, respectively.

### 2.2. Characterization

The morphologies of $Bi_{25}FeO_{40}$/rGO nanocomposites were observed *via* scanning electron microscopy (SEM, S-4800, Hitachi; accelerating voltage = 8 kV). The obtained samples were characterized by XRD on a Bruker D8 Advance X-ray powder diffractometer with Cu Kα radiation ($\lambda = 1.5418$ Å) in the $2\theta$ range of 20° to 60° with a step size of 0.002° and a scan speed of 0.5 second per step. The accelerating voltage and the applied current were 40 kV and 40 mA, respectively. UV-vis absorption spectra were obtained using a PerkinElmer Lambda 35 spectrophotometer. The XPS spectrum was recorded on the Thermo Scientific ESCALAB 250Xi X-ray photoelectron spectrometer. The specific surface area was determined by V-Sorb 2800P (Gold APP Instruments Corporation, China) through the BET method.

### 2.3. Photocatalytic tests

The photocatalytic activities of $Bi_{25}FeO_{40}$/rGO nanocomposites were evaluated by degradation of MO aqueous solution under visible light irradiation. A 500 W Xe lamp was used as the light source, and visible-light irradiation was realized by attaching a 420 nm cutoff filter to completely remove any radiation below 420 nm. In a typical photocatalytic test, 50 mg catalyst was dispersed in 50 mL MO aqueous solution with a concentration of 5 mg $L^{-1}$. Prior to irradiation, the suspensions were magnetically stirred in the dark for 1 h to ensure the establishment of an adsorption–desorption equilibrium. Then, at selected time intervals of 30 min, samples were collected and filtered to remove the photocatalyst particles by centrifugation. After that, the solution was analyzed using an ultraviolet-visible light spectrophotometer. A blank test was also carried out on an aqueous MO solution without photocatalyst under the same condition.

## 3. Results and discussion

### 3.1. Characterization of samples

The morphology of $BiFeO_3$ nanostructures were assessed by SEM, as depicted in Fig. 1. From Fig. 1a, it can be easily found that $BiFeO_3$ is comprised of many spindle-like particles with relatively uniform size distribution. The high magnification SEM images displayed in Fig. 1b showed that the $BiFeO_3$ spindles are consist of large amounts of small particles and the surfaces are quite rough. The width and length of those spindle-like particles are *ca.* 200 nm and *ca.* 400 nm, respectively.

The crystal phase of the photocatalysts is determined by XRD, as shown in Fig. 2. For $BiFeO_3$ without rGO added, the diffraction peaks can be indexed on the basis of a $BiFeO_3$ rhombohedral phase with the space group *R*3*c* (JCPDS card no. 86-1518), a slight impurity phases can be observed. Interestingly, the presence of rGO in $Bi_{25}FeO_{40}$/rGO nanocomposites preferentially induces the formation of the sillenite-type phase of $Bi_{25}FeO_{40}$ (JCPDS card no. 46-0416). $Bi_{25}FeO_{40}$ is an important member of the ternary metal oxides with a body-centered cubic crystal structure (space group *I*23 with cell parameter of about 1.018 nm).[29] Previous report has proved the existence of dipole moment in the $Bi_{25}FeO_{40}$ crystal structure, which may enhance the electron–hole separation.[30] Thanks to high content of acidic oxygen-containing functionality, the presence of rGO could resulted in affected acidity of the aqueous solution, which eventually suppressed the generation of iron oxide.[31] Jiang *et al.* have found that sillenite-type phase $Bi_{25}FeO_{40}$ with a relatively low Fe content was obtained. Hence, sillenite-type phase $Bi_{25}FeO_{40}$ was preferentially formed.

After hybridization of rGO, the rhombohedral $BiFeO_3$ phase disappeared and transformed to the sillenite $Bi_{25}FeO_{40}$ phase.

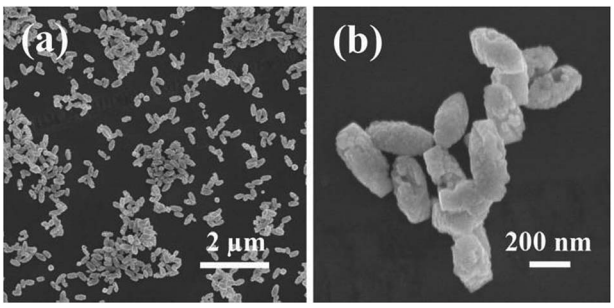


Fig. 1 SEM images with different magnifications of the $BiFeO_3$ nanostructures.

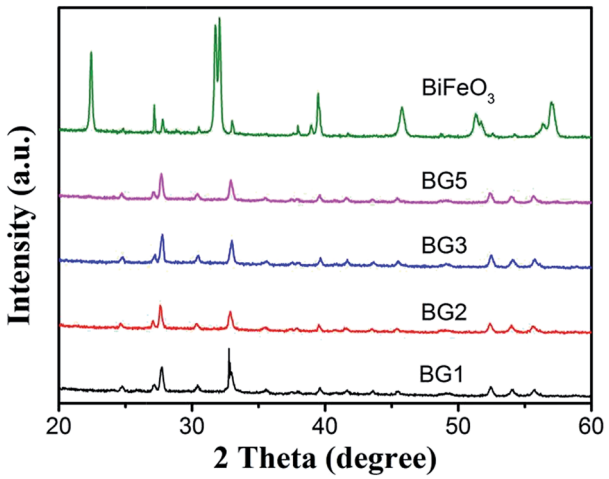


Fig. 2 XRD patterns of $BiFeO_3$ and various $Bi_{25}FeO_{40}$/rGO nanocomposites.

Interestingly, the morphology of $Bi_{25}FeO_{40}$ kept well. The SEM images of $Bi_{25}FeO_{40}$/rGO nanocomposites are displayed in Fig. 3. The spindle-like $Bi_{25}FeO_{40}$ nanoparticles were randomly attached to the surface of rGO nanosheets which resemble crumpled silk veil waves. When adding rGO, the agglomeration of $Bi_{25}FeO_{40}$ can be effectively avoided. The images also imply that more and more spindles located at the nanosheets surface while continuously increasing the amount of $BiFeO_3$ powders in the synthesis process. The $Bi_{25}FeO_{40}$ spindles maintained their highly irregular and rough surfaces, which can magnify the surface area of the catalyst resulting in higher photocatalytic activity.

Similar results are elucidated from TEM analysis, as shown in Fig. 4. The $Bi_{25}FeO_{40}$ spindles dispersed well in the rGO matrix which consist of corrugated and transparent sheets. The rGO nanosheets, where spindles are wrapped in, preferred to

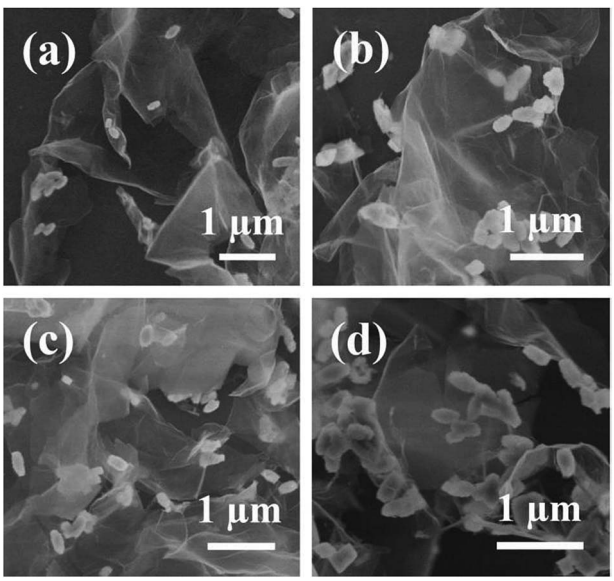


Fig. 3 SEM images of the $Bi_{25}FeO_{40}$/rGO nanocomposites. (a) BG1, (b) BG2, (c) BG3 and (d) BG5.

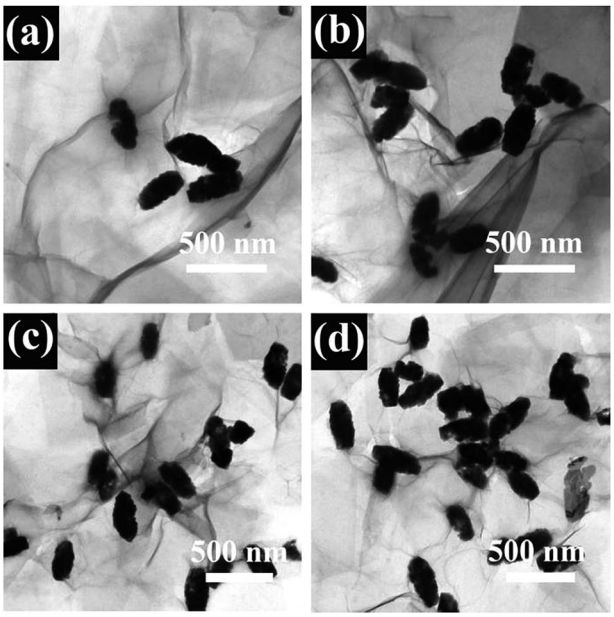


Fig. 4 TEM images of the $Bi_{25}FeO_{40}$/rGO nanocomposites. (a) BG1, (b) BG2, (c) BG3 and (d) BG5.

wrinkle up. It clearly showed that the $Bi_{25}FeO_{40}$ spindles featured a size of 300–400 nm anchored uniformly on both sides of the rGO nanosheets. Some $Bi_{25}FeO_{40}$ spindles were encapsulated within the rGO sheets, which can efficiently prevent the aggregation of particles. The results also revealed rGO as a rather thin microstructure, which enhanced the specific surface ratio.[32] The rGO nanosheets interconnected with each other to form an open pore system, which suppressed the dissolution and agglomeration of particles, thereby promoting the stability of the composites.[33,34]

In order to confirm the valence of some elements in the products, XPS analyses were carried out. Fig. 5a shows a typical wide-scan XPS spectrum, in which all peaks can be assigned to Bi, Fe, O and C elements. Fig. 5b depicts the fine XPS spectrum of Bi 4f, the peaks at 159.3 eV and 164.5 eV can be attributed to the binding energies of Bi $4f_{7/2}$ and Bi $4f_{5/2}$ in $Bi_{25}FeO_{40}$, which reveal that Bi is in the $Bi^{3+}$ oxidation state. As shown in Fig. 5c, the Fe 2p spectra doublet consist of two peaks of Fe $2p_{3/2}$ (710.7 eV) and Fe $2p_{1/2}$ (724.7 eV), which corresponding to the characteristics of $Fe^{3+}$ ions. In Fig. 5d, the peak of O 1s at 530.1 eV and 532.5 eV should be assigned to the binding energies of O in the Fe–O and Bi–O chemical bonds, respectively.

### 3.2. Optical and photocatalytic performance

The optical properties of the as-prepared $Bi_{25}FeO_{40}$/rGO nanocomposites were measured by UV-vis diffuse reflectance spectroscopy (DRS). As can be seen from Fig. 6, all the samples showed strong and broad absorption in the range of 350–600 nm, which indicated that $Bi_{25}FeO_{40}$/rGO nanocomposites could response to visible light. It can be seen that the absorbance peak in the visible region of BG3 samples is stronger than that of the other nanocomposites. Furthermore, the absorption

 

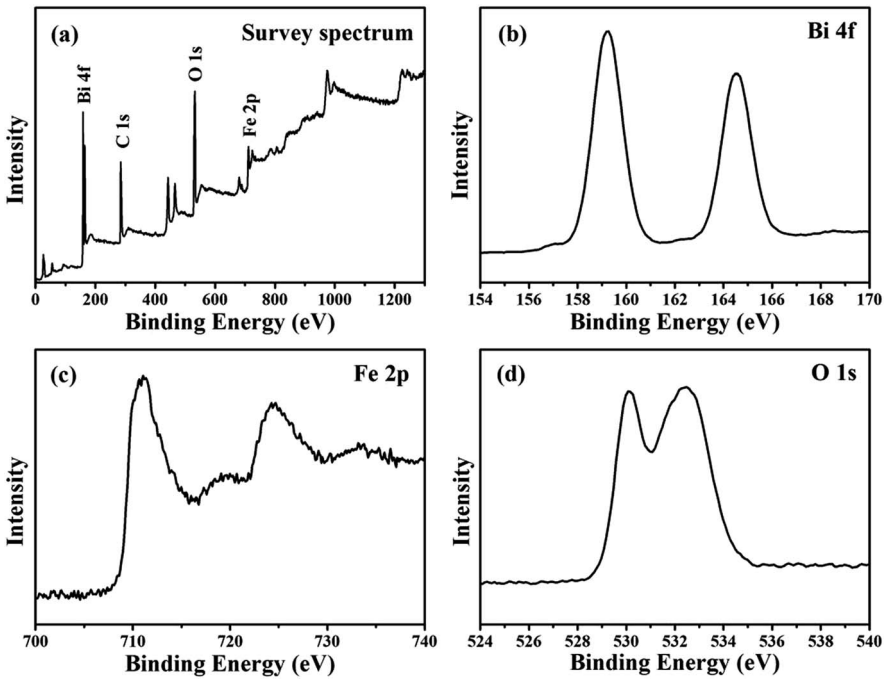


Fig. 5 The XPS spectra of (a) full survey of $Bi_{25}FeO_{40}$/rGO, (b) Bi 4f core levels of $Bi_{25}FeO_{40}$/rGO, (c) Fe 2p core levels of $Bi_{25}FeO_{40}$/rGO and (d) O 1s core levels of $Bi_{25}FeO_{40}$/rGO.

spectrum of the BG3 sample shows an obvious red-shift trend compared with that of other samples.

The photocatalytic degradation of methyl orange (MO) aqueous solution under visible light irradiation was detected to evaluate the photocatalytic performance of $Bi_{25}FeO_{40}$/rGO nanocomposites and the results are shown in Fig. 7. The suspension was placed in the dark for 1 h with magnetic stirring before irradiation to reach the adsorption/desorption equilibrium. It is observed that MO degradation is negligible in the absence of the photocatalyst. The photocatalytic degradation efficiencies are calculated to be 48% for $BiFeO_3$ after three hours of irradiation. By comparison, the degradation efficiency of $Bi_{25}FeO_{40}$/rGO nanocomposites is increased to 74% for BG1 and reaches the maximum value of 88% for BG3 under the same experimental conditions, which are much higher than the pure $BiFeO_3$ photocatalyst. The enhancement of the photocatalytic performance should be mainly ascribed to the increase of the light absorption in the $Bi_{25}FeO_{40}$/rGO nanocomposites for the interfacial structure,[35–37] which can reduce the recombination rate of photogenerated electrons and holes.

In addition to the photocatalytic efficiency, the stability and recyclability of a photocatalyst was also very important from the point of view of its practical application. The sample of BG3 was selected to evaluate the reusability under the same reaction

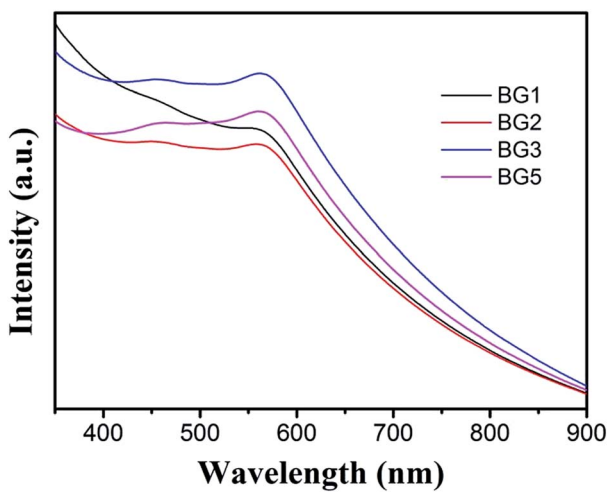


Fig. 6 UV-vis absorption spectra of $Bi_{25}FeO_{40}$/rGO nanocomposites.

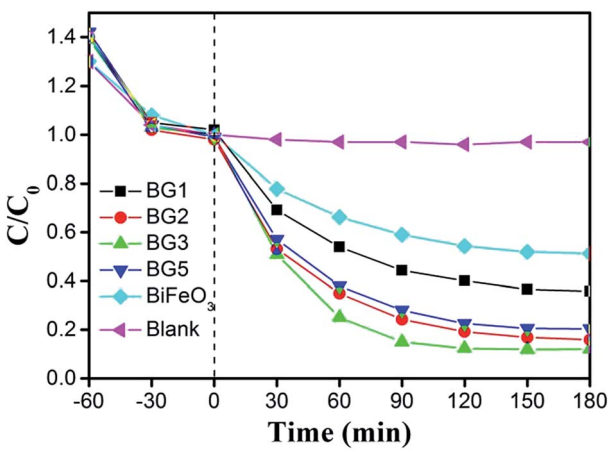


Fig. 7 Photocatalytic activity of different catalysts for the degradation of MO solution at room temperature.

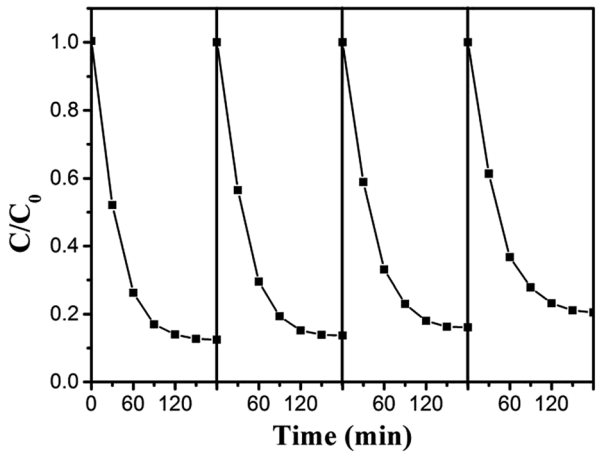


Fig. 8 Recyclability of the $Bi_{25}FeO_{40}$/rGO photocatalyst in four successive experiments for the photocatalytic degradation of MO under visible light irradiation.

conditions. From Fig. 8, the BG3 photocatalyst shows a good catalytic stability after four recycles. The slight decrease could be attributed to the inescapable loss of catalyst during the recycling process. The result indicated that photocatalysts based on $Bi_{25}FeO_{40}$/rGO nanocomposites could be reused completely for wastewater treatment.

Fig. 9 displays the photoluminescence (PL) spectra of the as-prepared $BiFeO_3$ and the $Bi_{25}FeO_{40}$/rGO nanocomposites excited by 568 nm. The main emission peak is centered at about 440 nm for the pure $BiFeO_3$ sample. Compared with $BiFeO_3$, the PL spectra intensity of the $Bi_{25}FeO_{40}$/rGO nanocomposites is significantly decreased in the same position, which indicated that the photogenerated charges recombination rate in $Bi_{25}FeO_{40}$/rGO composites was much lower than that in $BiFeO_3$ samples. That is, the photogenerated electron–hole pairs can efficiently transfer at the interface of $Bi_{25}FeO_{40}$/rGO composites, resulting in the highest photocatalytic activity under visible light irradiation.

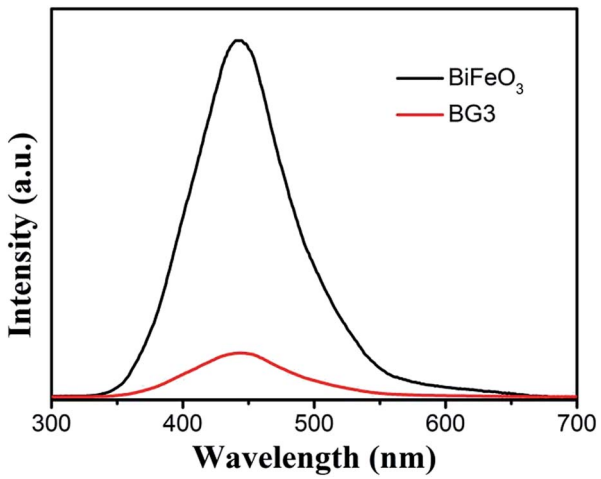


Fig. 9 PL spectra of the as-prepared $BiFeO_3$ and the $Bi_{25}FeO_{40}$/rGO nanocomposites.

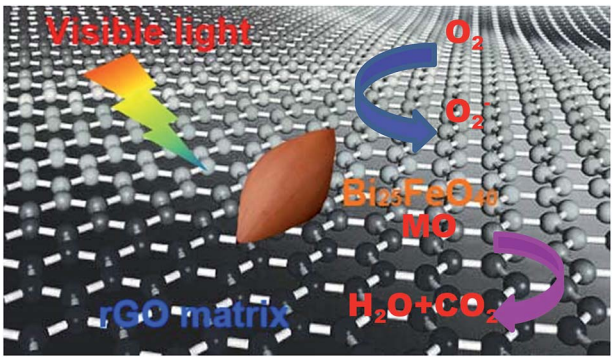


Fig. 10 The proposed photocatalytic mechanism for MO degradation over the $Bi_{25}FeO_{40}$/rGO nanocomposites.

The enhancement of the photocatalytic activity should be mainly attributed to the increase of the light absorption and the synergistic effect in the $Bi_{25}FeO_{40}$/rGO nanocomposites, a proposed mechanism is discussed as shown in Fig. 10. Under visible light irradiation, $Bi_{25}FeO_{40}$ and rGO can be excited to create free electrons and holes. The photogenerated electrons in $Bi_{25}FeO_{40}$/rGO can easily move towards the surface of rGO sheets. The conjugated $sp^2$-hybridized structure of rGO composite materials provides abundance of delocalized electrons to enhance the transport of photogenerated electrons.[38] Accordingly, the superoxide anion radicals are formed in rGO sheets by a reaction between photoinduced electrons and adsorbed oxygen, while the hydroxyl radicals are formed in the $Bi_{25}FeO_{40}$ surface by a reaction between photoinduced holes and water.[39] Hence, MO molecules were degraded by serials reactions with holes, superoxide anion radical and hydroxyl radical.[31] One other important role in enhancing the photocatalytic efficiency is the surface area of catalyst. The specific surface area for BG3 was determined by BET (Brunauer–Emmett–Teller) measurements and the result showed that the specific surface area is 7.945 $m^2\ g^{-1}$. The effective surface area which organic dyes are in direct contact with catalyst could increase the adsorption of holes. $Bi_{25}FeO_{40}$ nanoparticles are well spread over the rGO sheets with very minor agglomeration, as shown in Fig. 4. As a result, the photogenerated electrons and holes are efficiently separated between $Bi_{25}FeO_{40}$ and rGO, which reduces the electron–hole recombination in the hybrid composite photocatalysts.[40] Meanwhile, $O_2$ absorbed on the surface of rGO could capture $e^-$ and form $^{\bullet}O_2^-$ which then oxidized MO directly on the surface. Both of these two predominance lead to an increase in the photo-conversion efficiency of the hybridized photocatalyst.

## 4. Conclusions

In conclusion, $Bi_{25}FeO_{40}$/rGO photocatalysts with varied $Bi_{25}FeO_{40}$ contents were synthesized by a liquid phase approach. At room temperature, a phase transition from rhombohedral $BiFeO_3$ to sillenite $Bi_{25}FeO_{40}$ took place with adding rGO in the solution, while the spindle-like structures were maintained after the reaction. The improved photo-degradation activity toward methyl

orange can be mainly ascribed to the structural characteristics of sillenite type $Bi_{25}FeO_{40}$ and the great charge mobility of rGO, which retard the recombination of photoexcited pairs. Therefore, the $Bi_{25}FeO_{40}$/rGO nanocomposite is a promising photocatalytic material for environmental applications as well as water splitting.

## Acknowledgements

We acknowledge the financial support from the Ministry of Education of China (No. IRT1148), Jiangsu Synergistic Innovation Center for Advanced Materials (SICAM), the Project Funded by the Priority Academic Program Development of Jiangsu Higher Education Institutions (PAPD, YX03001), the National Natural Science Foundation of China (51372119, 61377019, 61136003, 51173081, 51602161), College Postgraduate Research and Innovation Project of Jiangsu Province (KYLX_0794, KYLX15_0848), the Natural Science Foundation of Jiangsu Province (KZ0070715050), the Seed Project Funded by Introducing Talent of NJUPT (XK0070915022) and the Natural Science Foundation of NJUPT (NY214129, NY214130, NY214181, NY215176, NY215077).

## Notes and references

1 J. Wang, J. B. Neaton, H. Zheng, V. Nagarajan, S. B. Ogale, B. Liu, D. Viehland, V. Vaithyanathan, D. G. Schlom, U. V. Waghmare, N. A. Spaldin, K. M. Rabe, M. Wuttig and R. Ramesh, *Science*, 2003, **299**, 1719–1722.
2 B. Sun and C. M. Li, *Phys. Chem. Chem. Phys.*, 2015, **17**, 6718–6721.
3 D. P. Dutta, O. D. Jayakumar, A. K. Tyagi, K. G. Girija, C. G. S. Pillaia and G. Sharma, *Nanoscale*, 2010, **2**, 1149–1154.
4 S. V. Vijayasundaram, G. Suresh, R. A. Mondal and R. Kanagadurai, *J. Alloys Compd.*, 2016, **658**, 726–731.
5 W. W. Mao, X. F. Wang, Y. M. Han, X. A. Li, Y. T. Li, Y. F. Wang, Y. W. Ma, X. M. Feng, T. Yang, J. P. Yang and W. Huang, *J. Alloys Compd.*, 2014, **584**, 520–523.
6 W. W. Mao, X. F. Wang, L. Chu, Y. Y. Zhu, Q. Wang, J. Zhang, J. P. Yang, X. A. Li and W. Huang, *Phys. Chem. Chem. Phys.*, 2016, **18**, 6399–6405.
7 T. Choi, S. Lee, Y. J. Choi, V. Kiryukhin and S. W. Cheong, *Science*, 2009, **324**, 63–66.
8 Z. X. Li, Y. Shen, Y. H. Guan, Y. H. Hu, Y. H. Lin and C. W. Nan, *J. Mater. Chem. A*, 2014, **2**, 1967–1973.
9 F. Gao, X. Y. Chen, K. B. Yin, S. Dong, Z. F. Ren, F. Yuan, T. Yu, Z. Zou and J. M. Liu, *Adv. Mater.*, 2007, **19**, 2889–2892.
10 J. An, L. Zhu, N. Wang, Z. Song, Z. Yang, D. Du and H. Tang, *Chem. Eng. J.*, 2013, **219**, 225–237.
11 Z. X. Li, Y. Shen, C. G. Yang, Y. C. Lei, Y. H. Guan, Y. H. Lin, D. B. Liu and C. W. Nan, *J. Mater. Chem. A*, 2013, **1**, 823–829.
12 B. Sun, L. J. Wei, H. W. Li and P. Chen, *J. Mater. Chem. C*, 2014, **2**, 7547–7551.
13 X. F. Wang, W. W. Mao, J. Zhang, Y. M. Han, C. Y. Quan, Q. X. Zhang, T. Yang, J. P. Yang, X. A. Li and W. Huang, *J. Colloid Interface Sci.*, 2015, **448**, 17–23.
14 M. Ahmadzadeh, A. Ataie and E. Mostafavi, *J. Alloys Compd.*, 2015, **622**, 548–556.
15 Y. Q. Zheng, G. Q. Tan, H. Y. Miao, A. Xia and H. J. Ren, *Mater. Lett.*, 2011, **65**, 1137–1140.
16 Z. X. Li, Y. Shen, Y. H. Guan, Y. H. Hu, Y. H. Lin and C. W. Nan, *J. Mater. Chem. A*, 2014, **2**, 1967–1973.
17 X. Yang, G. Xu, Z. H. Ren, X. Wei, C. Y. Chao, S. Y. Gong, G. Shen and G. R. Han, *CrystEngComm*, 2014, **16**, 4176–4182.
18 M. T. Borowiec, A. Majchrowski, J. Zmija, H. Szymczak, T. Zayarniuk, E. Michalski and M. Baranski, *Solid State Crystals 2002: Proc. SPIE*, 2003, vol. 5136, pp. 26–30.
19 J. M. Li, J. Y. Song, J. G. Chen, S. W. Yu, D. R. Jin and J. R. Cheng, *Mater. Res. Soc. Symp. Proc.*, 2010, **1217**, 1217.
20 L. Zhang, X. Zhang, Y. Zou, Y. H. Xu, C. L. Pan, J. S. Hu and C. M. Hou, *CrystEngComm*, 2015, **17**, 6527–6537.
21 L. Zhang, Y. Zou, J. Song, C. L. Pan, S. D. Sheng and C. M. Hou, *RSC Adv.*, 2016, **6**, 26038–26044.
22 G. Q. Tan, Y. Q. Zheng, H. Y. Miao, A. Xia and H. J. Ren, *J. Am. Ceram. Soc.*, 2012, **95**, 280–289.
23 X. F. Wang, W. W. Mao, Q. X. Zhang, Q. Wang, Y. Zhu, J. Zhang, T. Yang, J. P. Yang, X. A. Li and W. Huang, *J. Alloys Compd.*, 2016, **667**, 288–293.
24 P. Li, Q. Chen, Y. Y. Lin, G. Chang and Y. B. He, *J. Alloys Compd.*, 2016, **672**, 497–504.
25 Y. H. Li, Y. J. Sun, F. Dong and W. K. Ho, *J. Colloid Interface Sci.*, 2014, **436**, 29–36.
26 Y. Zhou, X. J. Zhang, Q. Zhang, F. Dong, F. Wang and Z. Xiong, *J. Mater. Chem. A*, 2014, **2**, 16623–16631.
27 T. Xiong, F. Dong, Y. Zhou, M. Fu and W. K. Ho, *J. Colloid Interface Sci.*, 2015, **447**, 16–24.
28 W. S. Hummers and R. E. Offeman, *J. Am. Chem. Soc.*, 1958, **80**, 1339.
29 Y. Du, Z. Cheng, Z. Yu, S. X. Dou, X. Wang and L. Q. Liu, *J. Nanosci. Nanotechnol.*, 2012, **12**, 1684–1687.
30 J. B. Lu, Y. Dai, Y. T. Zhu and B. B. Huang, *ChemCatChem*, 2011, **3**, 378–385.
31 A. W. Sun, H. Chen, C. Y. Song, F. Jiang, X. Wang and Y. S. Fu, *RSC Adv.*, 2013, **3**, 4332–4340.
32 L. K. Pan, X. J. Liu, Z. Sun and C. Q. Sun, *J. Mater. Chem. A*, 2013, **1**, 8299–8326.
33 Z. S. Wu, Y. Sun, Y. Z. Tan, S. B. Yang, X. L. Feng and K. Müllen, *J. Am. Chem. Soc.*, 2012, **134**, 19532–19535.
34 L. Xiao, D. Q. Wu, S. Han, Y. S. Huang, S. Li, M. Z. He, F. Zhang and X. L. Feng, *ACS Appl. Mater. Interfaces*, 2013, **5**, 3764–3769.
35 K. Woan, G. Pyrgiotakis and W. Sigmund, *Adv. Mater.*, 2009, **21**, 2233–2239.
36 A. S. Zhu, Q. D. Zhao, X. Y. Li and Y. Shi, *ACS Appl. Mater. Interfaces*, 2014, **6**, 671–679.
37 S. Cong and Y. Xu, *J. Phys. Chem. C*, 2011, **115**, 21161–21168.
38 S. M. Sun and W. Z. Wang, *RSC Adv.*, 2014, **4**, 47136–47152.
39 Y. Wu, H. J. Luo, X. L. Jiang, H. Wang and J. J. Geng, *RSC Adv.*, 2015, **5**, 4905–4908.
40 L. Y. Huang, H. Xu, Y. P. Li, H. M. Li, X. N. Cheng, J. X. Xia, Y. G. Xu and G. B. Cai, *Dalton Trans.*, 2013, **42**, 8606–8616.